ACS OMEGA

http://pubs.acs.org/journal/acsodf

Article

Methodological Issues in First-Principle Calculations of $CH_3NH_3PbI_3$ Perovskite Surfaces: Quantum Confinement and Thermal Motion

Lucas Lodeiro,* Felipe Barría-Cáceres, Karla Jiménez, Renato Contreras, Ana L. Montero-Alejo,* and Eduardo Menéndez-Proupin*

Cite This: *ACS Omega* 2020, 5, 29477−29491

Read Online

ACCESS | Metrics & More | Article Recommendations | Supporting Information

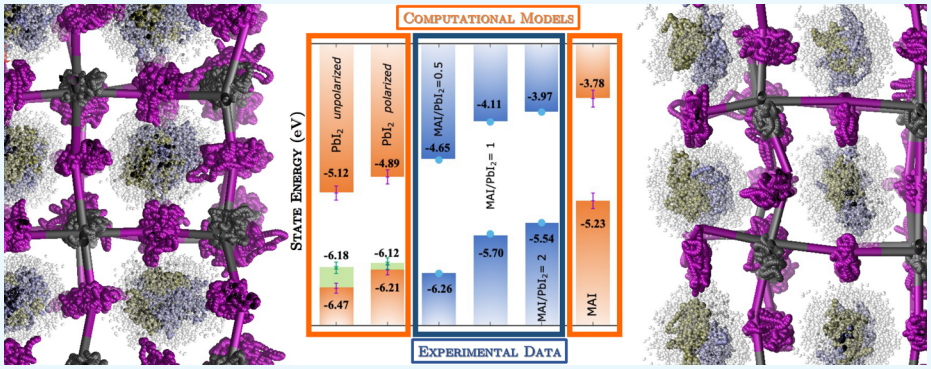

ABSTRACT: Characterization and control of surfaces and interfaces are critical for photovoltaic and photocatalytic applications. In this work, we propose $CH_3NH_3PbI_3$ (MAPI) perovskite slab models whose energy levels, free of quantum confinement, explicitly consider the spin−orbit coupling and thermal motion. We detail methodological tools based on the density functional theory that allow achieving these models at an affordable computational cost, and analytical corrections are proposed to correct these effects in other systems. The electronic state energies with respect to the vacuum of the static MAPI surface models, terminated in PbI_2 and MAI atomic layers, are in agreement with the experimental data. The PbI_2-terminated slab has in-gap surface states, which are independent of the thickness of the slab and also of the orientation of the cation on the surface. The surface states are not useful for alignments in photovoltaic devices, while they could be useful for photocatalytic reactions. The energy levels calculated for the MAI-terminated surface coincide with the widely used values to estimate the MAPI alignment with the charge transport materials, i.e., −5.4 and −3.9 eV for valence band maximum and conduction band minimum, respectively. Our study offers these slab models to provide guidelines for optimal interface engineering.

INTRODUCTION

Hybrid halide perovskites (HHPs) are a family of original semiconductor materials, and HHP solar cells under research achieve efficiencies that compete with silicon photovoltaic cells.[1] The semiconductor-unique features include long carrier diffusion lengths, low recombination losses, low material cost, and band gap-tuning capacity. Optimizing interfaces is one of the critical tasks that has a direct effect on the performance of solar cells.[2] The selection of optimal interfaces should consider commensurable vectors to avoid stress, favorable atomic junctions that prevent dangling bonds, and finally, barrier-free charge transport, i.e., electronic states aligned between both materials. Therefore, a first step to the correct design of an interface requires knowing details of the structure and energy of the states of each part.

Experimental advances have been critical to produce HHP thin films with the required degree of crystallinity to provide high cell performance. However, in the practice of building these solar cells, very little information is available on the characteristics of the surfaces obtained, neither their composition nor their energy levels. The same is true for their interfaces. By reviewing the electronic energy levels of perovskite films, determined essentially by combining ultraviolet photoelectron spectroscopy (UPS) and inverse photoemission spectroscopy (IPES), it is possible to realize that the reports differ greatly.[3] The differences are associated not only with the preparation methods and the ratio of precursors but also with the substrates and the exposure of the prepared films, air, light, and the thermal conditions.[2,3] Particularly in the

Received: September 9, 2020
Accepted: October 21, 2020
Published: November 9, 2020

methylammonium lead iodide perovskite (MAPI, MA^+ = $CH_3NH_3^+$), the HHP prototype, variations of up to 0.7 eV in energy levels are reported, changing the ratio of their precursors. However, most of the studies looking for alignments with MAPI levels still consider the reported VBM energy for bulk (−5.4 eV) and project the CBM energy at −3.7 or −3.9 eV, depending on the band gap considered.[2−6]

By scanning tunneling microscopy (STM) and spectroscopy, it was possible to elucidate the atomic rearrangement of the surface and the density of state of the valence band of an ultrathin film of MAPI.[7] The measurements corresponded to the orthorhombic phase, and it was concluded that the surface ends in a layer rich in methylammonium iodide (MAI) in the plane (001), with two rearrangements of iodine coexisting. With this experiment, a real image of defects is shown for the first time, although large areas of the surface without defects are mostly observed. The computational model explains the influence of organic cations on the rearrangements of the observed atoms. The STM technique also provided the surface description of $MAPbBr_3$ and other HHP-mixed compositions.[8−10] However, in all cases, the information is limited to the low-temperature phase that is far from the experimental conditions in which the solar cells are manufactured.

The elemental composition of the MAPI surface obtained by X-ray photoelectron spectroscopy (XPS), under controlled humidity conditions, has recently been reported for photocatalytic applications.[11] The analysis indicates that below 35% humidity, the MAI-type composition of the surface predominates, and at higher humidity, the surface is a PbI_2 type. However, the authors found no photoconversion activity on the MAPI surface in humidity conditions above 35%. The report supports that the MAI-type surface exhibits photocatalytic behavior because moisture generates surface defects exposing surface lead atoms as active sites.

Prior to the STM[7] and XPS[11] results, theoretical models of the surfaces of each of the three MAPI phases had already been attained, including some defect proposals. For the orthorhombic phase, the (100) and (001) slab models appear with the lowest surface energies, which correlates with the largest coordination number of the surface Pb atoms.[12] In agreement to the subsequent STM experiment, the surfaces show MAI-type terminations, and the interactions between organic cations and iodine atoms are a stabilizing factor.

Surface models corresponding to a pseudo-cubic unit cell have also been anticipated, this time, to study the adsorption of a molecule that simulate hole transport layers in solar cells.[13] The slabs representative of the (001) surfaces included the MAI- and PbI_2-type terminations, both stoichiometric. Again, the orientation of the surface MA^+ influences the stabilization mechanism of the slabs. Binding energy calculations predict the preferred conformation of the adsorbed molecule on the surface, although energy level alignment was not considered.

The surface of the tetragonal phase has been more studied since it is the phase most stable at room temperature, and several stoichiometric and nonstoichiometric (with defects) models have been proposed.[6,14−17] These studies suggest that the MAI-terminated (110) and (001) surfaces are energetically favored, although PbI_2-type terminations are still possible. The greater stability of the MAI-terminated slab is again associated with the NH_3^+ group of MA^+ interacting with the iodine atoms, configuration where the CH_3 group is oriented outward, namely, top C.[17] The relative instability of the PbI_2-terminated surface at vacuum could favor its energy of adhesion with any transporting layers in the cell.[15]

In addition to the differences in the stability of the surface termination, reports show that electronic properties of each surface are highly sensitive to the size and the relative orientation of MA^+ within each slab. An initial report estimated the convergence in surface energy by modeling slabs up to five layers thick, where each layer extent is a half-unit cell.[15] The surface terminated by MAI did not reach convergence with respect to the band gap for these slab thickness, whereas the PbI_2-terminated surface revealed a constant band gap. Other models show that both the band gaps and the energies of the frontier states with respect to the vacuum level change if the CH_3 or NH_3^+ ends of the MA^+ are regularly oriented toward the vacuum or if an apolar configuration of these cations is imposed within the entire slab.[17] Despite finding these variations, the agreement between the calculated frontier electronic states and the experimental data was reasonably achieved including spin−orbit coupling (SOC) effects as *a posteriori* correction.

How to get accurate slab models? When surfaces and interfaces are studied by *ab initio* methods, computational cost restricts the slab thickness to a few nanometers, compared to the tens or hundreds of nanometers in experimental cases. In this quantum well regime, the electronic states are affected by quantum confinement. The correct description of the geometry and the electronic structure of the surface and the inside, requires a study of the convergence of certain parameters such as electronic state energies, surface energies and band gap, with respect to the thickness of the slab. Also, vacuum thickness is an important parameter when periodic boundary conditions are used for the three directions due to the fact that the model has replicas in the cleavage direction, and the vacuum needs to be long enough to avoid interaction with periodic replicas. In this work, we approach different computational methodologies in search of accurate representations of MAPI surfaces from slab models. The surface energy levels are modeled by means of a method that refers the band energies of the bulk to the energy levels of the slab, considering hybrid functional and SOC. Furthermore, the results were validated with the self-consistent wave function of sufficiently large slabs under the same level of theory. Correspondingly, the convergence of these energy levels with respect to the size of the slab and its corresponding vacuum layer is also studied. Finally, the surface structures have been characterized including thermal motion, so we can include features that static models cannot address. The displacement of the band edges due to thermal motion is quantified to finally discuss its implication in the alignment of MAPI bands with other materials.

MODELS AND COMPUTATIONAL METHODS

We modeled MAPI surfaces as slab models constructed by replication of the MAPI unit cell. We start from a model of the tetragonal crystal structure of $MAPbI_3$, which is a 48-atom unit cell, named *Unpol* in ref 18. The name *Unpol* refers to the null polarization associated to the orientation of the C−N bonds in all (001) MAI layers. This structure represents a polymorphic configuration of the phase since the distortions are similar to those obtained within the configurational ensemble of this phase including thermal motion.[18]

The *Unpol* unit cell was optimized by means of variable-cell relaxation. Total energies, forces, and stress tensors were

https://dx.doi.org/10.1021/acsomega.0c04420
ACS Omega 2020, 5, 29477−29491

obtained from density functional theory (DFT) calculations, as implemented in the Quantum ESPRESSO code.[19] Two exchange and correlation functionals were used, the improved generalized gradient approximation (GGA) PBEsol[20] and the nonlocal vdW correlation optB88-vdW[21,22] (vdW). These functionals have different strengths. Dispersion-corrected vdW functionals are essential to describe binding of layered materials and molecular crystals. Although their use is not mandatory for HHP, they allow to obtain lattice parameters in very excellent agreement with the experiment.[23,24] However, vdW functionals cannot be used with the SOC, which modifies the band structure of the HHP. Hybrid functionals, including a fraction of Hartree−Fock exchange, together with the SOC, allow to accurately describe the band structure of $CH_3NH_3PbI_3$.[23] However, the computational cost associated precludes its use in more computationally demanding simulation techniques like molecular dynamics. SOC is crucial to describe the conduction band minimum, which is composed mainly of Pb 6p atomic orbitals, and presents interesting effects like the Rashba splitting. An intermediate solution is in the PBEsol functional, which allows to obtain good lattice parameters, and can be combined with SOC to obtain suitable conduction bands. The main drawback of PBEsol is that the band gaps are still too low. Part of this problem can be overcome using the scissors operator or by expensive calculations using hybrid functionals.

The Brillouin zone was sampled using a Γ-centered 3 × 3 × 2 *k*-point grid. The volume deviation with respect to the experimental value[25] reached −3.6 and −0.2% for PBEsol and vdW functionals, respectively. The lattice vectors were orthogonalized, neglecting small deviations from right angles. The spin−orbit coupling was not included here because its effect on the geometries is insignificant. Details on cutoffs, convergence threshold, and pseudopotentials employed are given in the Supporting Information.

Slab models of MAPI(001) surfaces were obtained, cleaving bulk supercells at selected atomic planes with orientation (001). As shown in Figure 1, the simulation supercell contains a crystal volume (the slab) and a vacuum volume. The crystal volume is continuous in two directions, namely, *x* and *y*, and the surface is normal to the third direction, *z*. Periodic boundary conditions are used for the three directions. Therefore, these represent two infinite surfaces, which must be sufficiently separated not to interact. The separation of the surfaces is determined by both the slab and vacuum thicknesses, the effect of which will be studied in subsections Slab Thickness Convergence and Vacuum Width Convergence. In order to avoid using dipole correction, the slabs and their surfaces were constructed and relaxed, canceling the dipoles presented in surfaces,[26,27] mainly, by MA^+ rotations (see in subsection Surface Structure and Thermal Motion). We did not enforce the use of symmetry elements (mirror planes, inversion, for example) on the calculation, albeit the crystal geometry remained very close to its symmetric structure, which presents these elements of symmetry.

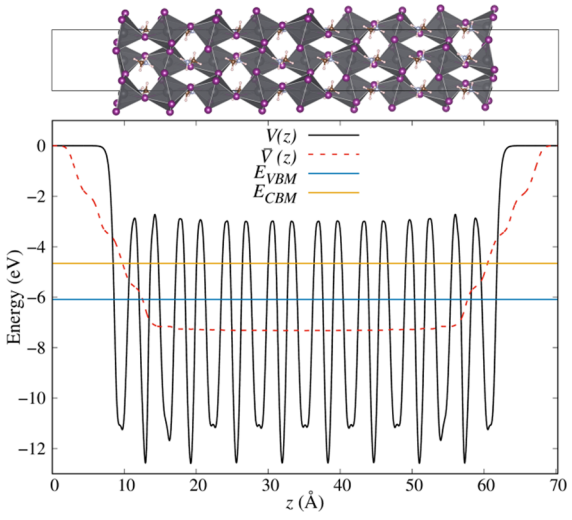

Figure 1. Planar averaged ($V(z)$) and macroscopic ($\bar{V}(z)$) electrostatic potentials, VBM and CBM energies with respect to the vacuum level for the (1 × 1) × 8 MAPI(001)-PbI_2 slab computed with PBEsol.

Let us define the slab stoichiometric unit as a couple of adjacent MAI and PbI_2 (001) planes that span half of a unit cell with thickness $c/2$. Mind that $c/2$ roughly equals the lattice parameter of the cubic phase of MAPI. Henceforth, the number of stoichiometric units defines the slab thickness, as well as the number of MAI and PbI_2 planes. An additional PbI_2 or MAI plane was added to each slab in order to have two symmetric surfaces (breaking the system stoichiometry) and to avoid internal electric field. Hence, a MAPI(001)-PbI_2 slab of *n* stoichiometric units has a total of *n* MAI layers and *n* +1 PbI_2 layers, while for MAPI(001)-MAI, the numbers are permuted. The lattice vectors parallel to the surface can be linear combinations of the primitive vectors, allowing for surface reconstruction. Hence, we employ the slab nomenclature (*m* × *m*) × *n* for the slab models, where *m* indicates the unit cell multiplication in each orthogonal direction along the surface. The index *n* indicates the number of stoichiometric units along the direction [001].

All the atomic coordinates within the slabs were relaxed with the *a* and *b* cell vectors fixed at their bulk values. The cell vector perpendicular to the surface was also kept fixed, and its optimal value was studied in subsection Slab thickness convergence. The electronic state energies were computed for the (1 × 1) × *n* slab without and with the SOC, using a Γ-centered 3 × 3 × 1 *k*-point grid. With this setup, a convergence study was performed (subsection Vacuum Width Convergence) in order to set the optimal values of slab thickness and vacuum width.

Once the convergence criteria were established, the surface physical properties were studied using two, MAI- and PbI_2-terminated, (2 × 2) × 6 slabs with a vacuum width of 35 Å, and the Γ *k*-point. For these production slabs, the atomic coordinates were relaxed using the vdW functional. The GGA and vdW functionals seriously underestimate the band gaps and give erroneous values of the band energies, although the band gap error is fortuitously compensated when the SOC is not included.[23] To obtain accurate band energies in the bulk crystal, the HSE hybrid functional[28,29] was employed. The band edges were aligned with respect to the out-of-surface vacuum level using a two-step procedure explained in section Alignment with Respect to the Vacuum Level. In addition, self-consistent slab calculations with vdW and the HSE hybrid functional were performed with the VASP code.[30,31]

To assess the effect of thermal motion on the surface properties, *ab initio* molecular dynamics simulations were performed with the CP2K code,[32,33] for the (2 × 2) × 6 slabs. We took advantage of the efficiency of this code by using the

https://dx.doi.org/10.1021/acsomega.0c04420
ACS Omega 2020, 5, 29477−29491

hybrid Gaussian and plane wave method (GPW) to represent the wave functions and electronic density and the approach to extrapolate the density matrix implemented in the DFT QuickStep module.[34] Force evaluations were performed using the PBE functional with the Grimme correction scheme (DFT-D3) to account for vdW interactions.[35,36] The Born−Oppenheimer scheme, microcanonical ensemble, and periodic boundary conditions were used. Further details are given in the Supporting Information. The simulations started from the relaxed slab structures, with an initial temperature of 600 K. A time step of 0.5 fs was used to integrate the Newton equations of motion. The thermalization time was 5 ps. Afterward, the production runs were extended up to 40 ps.

ALIGNMENT WITH RESPECT TO THE VACUUM LEVEL

The energies of the valence band maximum (VBM) and the conduction band minimum (CBM), with respect to the vacuum level, are the negatives of the ionization potential (IP) and the electron affinity (EA), respectively. With DFT calculations, the VBM and CBM are usually determined by means of a two-step procedure.[37−39] First, the average electrostatic potential is obtained for the slab model, as shown in Figure 1 and Figure S2 for PbI_2 and MAI surfaces, respectively. From the slab calculation, the electrostatic potential $V(x, y, z)$ is extracted and analyzed by means of two kinds of averages. First, the planar-averaged electrostatic potential is given as

$$V(z) = \frac{1}{A_{xy}} \iint V(x, y, z)\, \mathrm{d}x\mathrm{d}y + E_0 \quad , \tag{1}$$

where A_{xy} is the transverse area of the slab. The constant E_0 is an energy shift applied to make $V(z) = 0$ in the vacuum region. In this way, the zero of energy is set to the electrostatic potential energy in vacuum. The vacuum reference determination is a current research topic.[40,41] Second, the convoluted macroscopic electrostatic potential is defined as

$$\overline{V}(z) = \frac{1}{c} \int_{-c/2}^{c/2} V(z + z')\, \mathrm{d}z' \quad , \tag{2}$$

where c is the lattice constant in the direction perpendicular to the slab surface. As $V(z)$ is periodic inside the crystal, $\overline{V}(z)$ should be constant at the central part of the slab. Also, $\overline{V}(z)$ is strictly constant and independent of the functional when it is computed for a unit cell of the crystal, i.e., without vacuum, as Figure 2 shows. The PBE0[42,43] hybrid functional was used in this case to compare. $\overline{V}(z)$ is precisely the reference used to transfer the VBM and CBM energies, from a three-dimensional (3D) crystal to a slab with vacuum. From a crystal calculation are obtained the average electrostatic potential $\overline{V}^{3D}$, and the energies E^{3D}_{VBM} and E^{3D}_{CBM}. Finally, the VBM and CBM energies with respect to the vacuum level are obtained as

$$E_\alpha = \overline{V}(z_{in}) + (E^{3D}_\alpha - \overline{V}^{3D}) \quad , \tag{3}$$

where α = VBM, CBM, and z_{in} is any point in the region of constant $\overline{V}(z)$ near the slab center, as shown in Figure 1.

This two-step process, with the difference $E^{3D}_\alpha - \overline{V}^{3D}$ transferred from a bulk calculation with a primitive cell, allows to correct the errors in VBM and CBM energies (leading to gap underestimation in GGA) by means of higher level calculations, such as hybrid functionals or the Green function method GW, over a primitive bulk cell. The slab calculation is prohibitively expensive with such high-level methods, but it can be done with GGA functionals, assuming that the electrostatic potential is well described by GGA. This assumption is true in most cases, also in MAPI, as demonstrated Figure 2 for non-SOC and SOC calculations with three functionals, over a bulk unit cell. Particularly, the different levels of theory and functionals do not change $\overline{V}(z)$ and $\overline{V}^{3D}$. There is just a little change in the $V(z)$ profile (<60 meV, as shown in Figure 2) due to little changes in electron density. SOC shifts electron density from MAI layers to the PbI_2 layer, while for both hybrid functionals, the shift is from the interlayer space to MAI and PbI_2 layers.

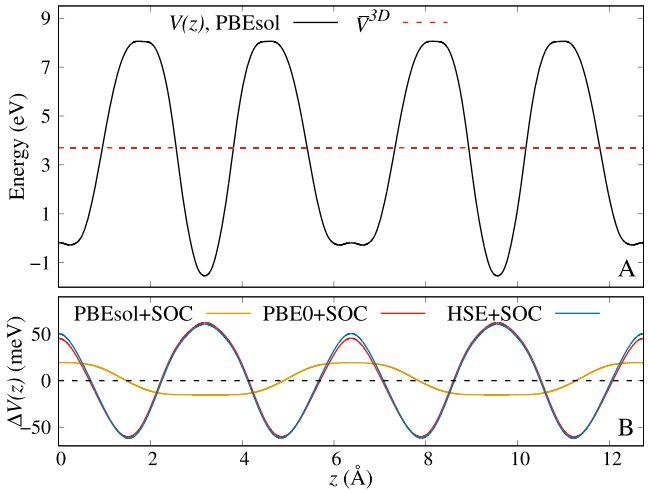

Figure 2. Planar-averaged and macroscopic electrostatic potential for the MAPI unit cell, along z, for different levels of theory and functionals. (A) PBEsol. (B) SOC and other functionals, as difference with respect to (A).

RESULTS AND DISCUSSION

Slab Thickness Convergence. In this subsection, we study the convergence of the electronic state energies, band gaps, surface energies, and structural parameters with respect to the slab. We have classified the different slab states, through inspection of spatial localization of squared wave functions, into surface states and bulk-confined states (VBM and CBM). The electronic states were studied at the Γ point, obeying the position of the bulk VBM and CBM (see the band-structure diagrams in Figure S1).

The first checked item was the convergence of the energy levels with respect to the slab thickness. Figure 3 shows, for MAPI(001)-PbI_2 and MAPI(001)-MAI slabs, the dependence of the frontier energy levels (relative to the vacuum level). The blue and sky-blue symbols correspond to the quantum confined states of CBM (top plot) and the VBM (bottom plot). The CBM is the lowest unoccupied crystal orbital (LUCO) for both surface types. In MAPI(001)-PbI_2, the higher occupied crystal orbital (HOCO) and the next (HOCO − 1) are surface states, which are doubly degenerate because this slab model has two equivalent surfaces. Thus, the VBM is the HOCO − 2. This is consistent with previous reports.[14] The surface states are caused by the cleavage of iodine octahedra around the surface Pb atom, which generates naked Pb atoms with dangled bonds. For MAPI(001)-MAI, the VBM-confined state is the HOCO, and no surface state has energy within the gap. The red and black symbols correspond

https://dx.doi.org/10.1021/acsomega.0c04420
ACS Omega 2020, 5, 29477−29491

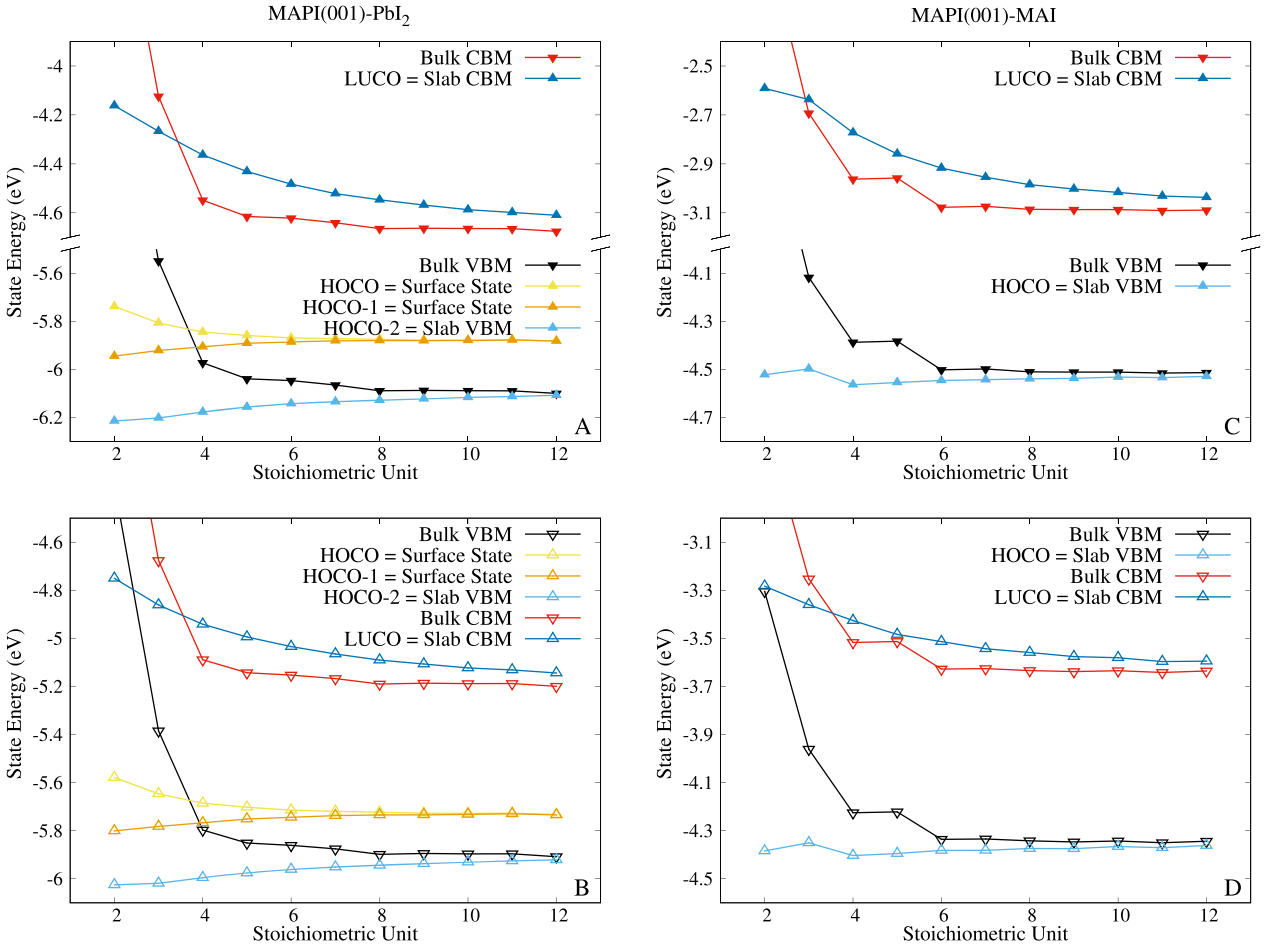

Figure 3. Convergence of energy slab levels, at the Γ point, with respect to slab thickness. (A, C) PBEsol. (B, D) PBEsol+SOC. Energies are with respect to the vacuum level.

to the CBM and VBM energies, respectively, obtained from the two-step procedure explained in section Alignment with Respect to the Vacuum Level. Its dependence with the slab thickness follows the behavior of the average electrostatic potential at slab center $\overline{V}(z_{in})$, from which they differ in constant values (eq 3).

Geng et al.[15] reported that the MAPI(001)-PbI_2 band gap depends weakly on slab thickness, also being smaller than the band gap of MAPI(001)-MAI. However, they did not identify the HOCO and HOCO − 1 in MAPI(001)-PbI_2 as surface states. This smaller band gap is consistent with our results (see Figure 4). Moreover, the surface state (HOCO) and CBM (LUCO) present a similar energy variation with respect to the slab thickness, leading to a nearly independent HOCO−LUCO gap (in the thinner slab thickness regime).

Figures S3 and S4 show several squared wave functions (HOCO, LUCO, etc.) and their energies for (1 × 1) × 8, MAPI(001)-PbI_2 and MAPI(001)-MAI, respectively, averaged like eq 1. Here, the surface characters of the HOCO and HOCO − 1 are clearly appreciated in the MAPI(001)-PbI_2 case. These states are localized mainly on the first PbI_2 layer. For the other states, the bulk character and the quantum confinement effect are clearly appreciated in Figures S3 and S4. In the envelope function approximation,[44] the band edge wave functions are products of Bloch functions (oscillating at the atomic scale) and slowly varying envelope function, which are of sinusoidal type in the quantum wells.[44] The envelope

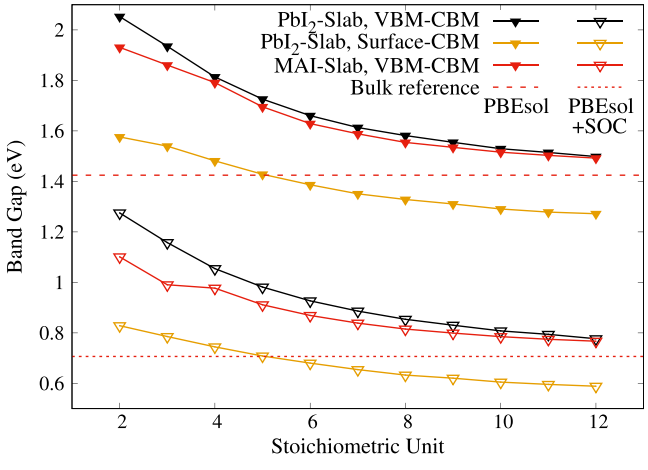

Figure 4. Convergence of MAPI(001)-PbI_2 and MAPI(001)-MAI band gaps (for inner slab bands and surface slab bands) with respect to slab thickness.

function tends to zero at the surface and has l nodes inside the slab for VBM − l and CBM + l states. There are also pseudo-nodes with smaller periodicity length along the slab due to the Bloch function oscillation.

We see that, regardless of surface termination, the variation of slab state energies due to quantum confinement with respect to the slab thickness (see Figure 3) is almost the same for non-

https://dx.doi.org/10.1021/acsomega.0c04420
ACS Omega 2020, 5, 29477−29491

SOC (top) and SOC (bottom) calculations. The main difference between non-SOC and SOC calculations (beyond states energies changes and decreased band gap) is in CBM (and higher states) squared wave function shapes. The SOC wave functions have smoother profiles.

The VBM- and CBM-confined states energies in Figure 3 exhibit quantum confinement behavior, as expected, in all cases. The CBM and VBM exhibit down (positive effective mass) and up (negative effective mass) energy shifts, respectively, for thicker slabs. While the energy convergence is faster in the VBM case, CBM presents quantum confinement even for the thickest calculated slab. This explains the VBM−CBM band gap overestimation (with respect to the bulk band gap) in all cases (see Figure 4). When $n < 4$, some VBM or CBM energies do not present smooth behavior, and the slabs are too thin to host bulk-like states. This shows that the bulk-inner slab description is poor at this regime. Also, the two-step procedure VBM and CBM are not well described in this ultrathin slab regime. For $n = 4$, the energies are roughly converged, and for $n \geq 6$, they are tightly converged, in all cases. The two-step procedure is, in principle, free of quantum confinement. This conception was checked, and for $n \geq 6$, the VBM and CBM present asymptotic behavior.

Finally, the surface states (MAPI(001)-PbI_2 slab models) exhibit energy splitting in the thinner regime. When the slab is sufficiently thick ($n = 6$ and $n = 7$ for non-SOC and SOC calculations, respectively), it is degenerated. This behavior shows that splitting is due to the surface state interaction (repulsion, like for the He_2 dimer) through the inner slab space and not through vacuum space.

The last parameter studied is the surface energy. Figure 5 displays the surface energy as a function of the slab thickness.

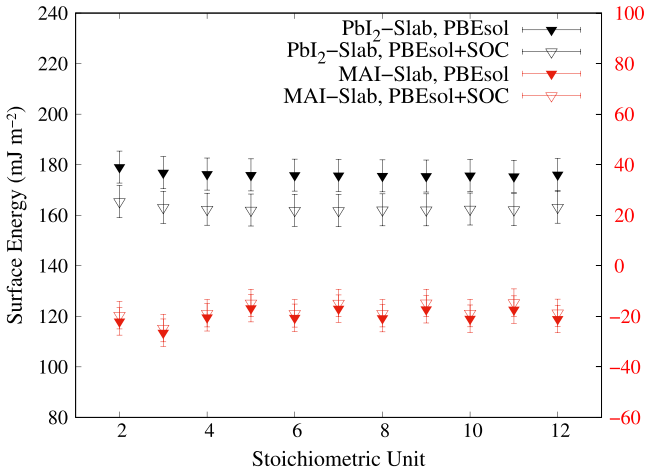

Figure 5. Convergence of MAPI(001)-PbI_2 and MAPI(001)-MAI surface energy with respect to slab thickness.

For a β = PbI_2- or MAI-surface type, this energy can be computed as

$$S_\beta^n = \frac{1}{2A_{xy}}\left(E_{\mathrm{slab},\beta}^n - \frac{n}{2}E_{\mathrm{MAPI}} - E_\beta\right) \quad , \tag{4}$$

where $E_{\mathrm{slab},\beta}^n$ is the total energy of an n-stoichiometric unit slab with two surfaces of type β, E_{MAPI} is the total energy of tetragonal bulk MAPI, and E_β is the total energy of solid bulk PbI_2 or MAI. The latter is the sum of chemical potentials of the out-of-stoichiometry species in a β-rich condition. The double surface counting is corrected with the 1/2 factor and normalized with respect to surface area A_{xy}.

The surface energy, for both surface types and for non-SOC and SOC calculations, is converged for all thicknesses, as shown in Figure 5. In the MAPI(001)-MAI case, the surface energy presents periodic oscillations for even and odd number of stoichiometric units. This is due to the existence of little dipole asymmetries between MA^+ in both surfaces, but these differences are within the error bars. About 80% of error is associated with the k-point grid, and the rest is associated with higher cutoff. Also, the negative value in surface energy is explained by MA^+ inversion and independent of the MAI bulk reference.[45−47] Before geometrical relaxation, the surface energy is positive as expected (∼110 mJ m^{-2}).

In the MAPI(001)-PbI_2 case, the surface energy behaves smoothly because both surfaces are highly symmetric for even and odd number of stoichiometric units. The higher surface energy in this case is explained by the contribution of surface states. We have used the PbI_2 bulk structure of ref 48. The inclusion of SOC in the calculations does not significantly change the surface energies for both surface types. SOC has a little effect in total energies, reinforcing not having included it in the atomic relaxation calculations. In the MAPI(001)-MAI case, the SOC effect is negligible. Meanwhile, in the MAPI(001)-PbI_2 case, surface energy has rigid downshifts. As this case has surface states located in Pb and I atoms (heavier atoms), it is understandable that SOC shifts are not totally negligible.

For all the thickness range considered, the geometrical parameters (see section Surface Structure and Thermal Motion) undergo minimal variations, matching the constancy of the surface energies.

Square Well Approximation. As has been discussed before, inner slab states present quantum confinement. They are 2-D delocalized states in the (001) plane but confined along the [001] direction (z axis). Moreover, the trends in the electronic state energies can be fitted with an infinite potential well model. Other considerations follow. The squared wave function envelopes, which modulate the Bloch functions, have sinusoidal behavior. The state energies' behavior seems consistent with a squared hyperbola curve, with asymptotic convergence at a high stoichiometric unit number. Also, the macroscopic electrostatic potential presents a pseudo-square well shape.

Blancon et al.[49] published a work on Ruddlesden−Popper halide perovskites, where the effect of the PbI_3 inorganic framework thickness was studied both experimentally and theoretically. These perovskites are dielectric well structures formed by two-dimensional layers of halide perovskite separated by butylammonium spacer layers. The optical absorption spectra of these dielectric wells (which are analogues to our thinnest vacuum-slab well models) exhibit lower exciton energies for thicker perovskite thickness. Also, these dielectric wells show the quantum confinement effect on band gaps.

Therefore, we propose the following analytical function, based on infinite potential well energies, to obtain the correct behavior relative to curvature and thickness dependence

$$E_\alpha(n) = \frac{\gamma}{\left(n\frac{c}{2} + 2\sigma\right)^2} + E_\alpha(\infty) \quad , \quad (n \geq 4) \tag{5}$$

https://dx.doi.org/10.1021/acsomega.0c04420
ACS Omega 2020, 5, 29477−29491

where $E_\alpha(n)$ is the state energy as a function of the number of stoichiometric units n, with α defined in Table 1. $\frac{c}{2}$ is the stoichiometric unit thickness (6.745 Å). γ, σ, and $E_\alpha(\infty)$, are the adjustable parameters. The first parameter, γ, is proportional to the curvature of the function. The second, σ, is a correction factor to account for the effect of non-infinite and a pseudo-square well. Finally, $E_\alpha(\infty)$ is the asymptotic value of state energy at infinite thickness. The parameter values are shown in Table 1. We used the confined state energy data from n = 4−12 for all fits.

Table 1. Fitted Eq 5 Parameters for VBM and CBM (Non-SOC and SOC Calculations)

α	γ (eV Å^2)	σ (Å)	$E_\alpha(\infty)$ (eV)
MAPI(001)-PbI_2			
CBM	+808.65	12.111	−4.690
VBM	−225.05	12.420	−6.088
CBM_{SOC}	+859.81	15.020	−5.219
VBM_{SOC}	−392.29	17.935	−5.891
MAPI(001)-MAI			
CBM	+439.55	5.682	−3.096
VBM	−97.64	10.965	−4.521
CBM_{SOC}	+338.31	7.218	−3.639
VBM_{SOC}	−181.56	16.131	−4.349

Figure S5 shows that the functions $E_\alpha(n)$ fit the data extremely accurately, where the root mean square of residues and $\overline{\chi}^2$ values are negligible, with orders of 10^{-3} and 10^{-5}, respectively.

The $E_\alpha(\infty)$ values show that the CBM (in all cases) exhibit quantum confinement even for the thickest slab models (n = 12), while the VBM are less affected, as previously discussed. Furthermore, the two-step process for $n \geq 4$ provides CBM and VBM energies close to $E_\alpha(\infty)$, showing faster convergence than the slab state energies.

The band gaps calculated from the asymptotic energy values without SOC are 1.40 and 1.43 eV for PbI_2 and MAI surfaces, respectively, which match the value 1.43 eV computed in the bulk system. With SOC, the asymptotic energy values are 0.67 and 0.71 eV for PbI_2 and MAI surfaces, respectively, matching the bulk value 0.71 eV.

The SOC correction (Δ_{SOC}) is defined as the difference between the SOC and non-SOC state energy function,

$$\Delta_{SOC}(n) = E_{\alpha_{SOC}}(n) - E_\alpha(n) \quad , \tag{6}$$

while the quantum confinement correction (Δ_{QC}) is defined as the difference between the asymptotic value of the state energy and the state energy function,

$$\Delta_{QC}(n) = E_\alpha(\infty) - E_\alpha(n) = \frac{-\gamma}{\left(n\frac{c}{2} + 2\sigma\right)^2} \quad . \tag{7}$$

Figures S6 and S7 show eqs 6 and 7, respectively, using data from Table 1. Δ_{SOC} presents near-constant behavior for all cases in the fitting range. Also, the Δ_{SOC} is practically equal to the value computed in the bulk system. Δ_{QC} is the negative of the quantum confinement energy.

This correction scheme allows to obtain the quantum confinement free state energies from a thin slab calculation performed with or without SOC.

Vacuum Width Convergence. The convergence of the state energies with respect to the width of the vacuum region was studied using n = 5 slabs, both for PbI_2 and MAI surfaces. We have considered three vacuum thicknesses: 6.4, 17.9, and 42.3 Å. To begin with, we have verified that the relaxed atomic positions do not change with the vacuum width. Figure 6 shows the behavior of the slab state energies and the macroscopic electrostatic potential ($\overline{V}(z_{in})$). The variations of all magnitudes are smaller than 20 meV, which is negligible. As shown in Figure S8, the surface energy variations are negligible (<0.2 mJ m^{-2}), being much smaller than the error bars.

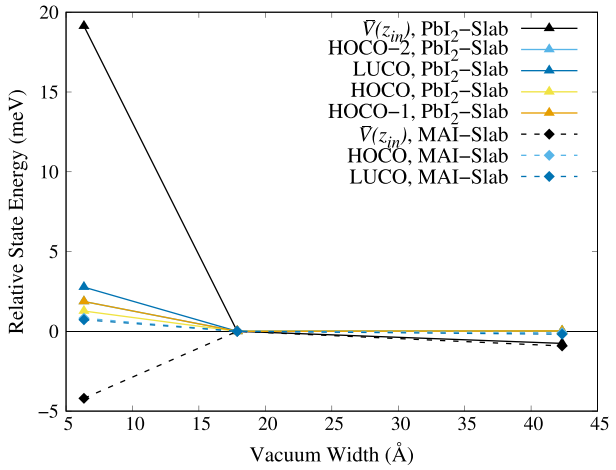

Figure 6. Convergence of MAPI(001)-PbI_2 and MAPI(001)-MAI state energies (in meV) with respect to vacuum thickness and relative to standard vacuum thickness.

Convergence Model Criteria. The previous subsections show the convergence studies for slab and vacuum thickness using a set of energetic and state variables. Here, we comment as a summary the most important results and their implications. In all slabs studied as MAPI(001) models, the VBM and CBM state energies present quantum confinement (greatest in CBM states), artificially increasing the band gap. We propose a correction scheme (Δ_{SOC} and Δ_{QC}), based on the square well approximation, to obtain energies of quantum confinement free states. The MAPI(001)-PbI_2 models exhibit occupied surface states caused by cleavage of a surface iodine octahedron, which triggers a reduction in band gap. The state energies obtained through the two-step process depend on the macroscopic electrostatic potential, and this parameter rapidly converges with the slab thickness. According to this method, the slab requires a minimum thickness of n = 4, but n = 6 is considered the optimal thickness to obtain state energies numerically close to the converged eigenvalues. The two-step process does not show the existence of in-gap surface states. The surface energies depend weakly on the slab thickness. Also, all parameters present weak dependence with the vacuum width.

Surface Structure and Thermal Motion. It is well known that distortion effects suffered by MAPI perovskites, unlike the low-temperature orthorhombic phase, should be considered to adequately estimate their electronic properties. Many times, the calculations show that a single conformation, usually those with greater symmetry, unequivocally represents the minimum of internal energy. However, thermal motion actually breaks this symmetry, and the system must be represented by a set of distorted conformations representative of the phase.

https://dx.doi.org/10.1021/acsomega.0c04420
ACS Omega 2020, 5, 29477−29491

We simulate dynamic trajectories of the (2 × 2) × 6 slabs, and with them we assess the distortions by thermal motion. Starting at 600 K in the microcanonical ensemble, our surface models reach equilibrium at 291 and 294 K for MAPI(001)-PbI_2 and MAPI(001)-MAI slabs, respectively. With these trajectories, we were able to evaluate the structure of the surfaces, validate our supercell models obtained at 0 K, and calculate the band edge shifts from representative structures of the tetragonal phase surfaces. Finally, we also verify if a small deformation in the *ab* plane of the slab models could affect the band edge states.

We begin the analysis, verifying that both static (0 K) and dynamic slab models preserve the tetragonal phase in the slab interior. As explained in ref 24, the tetragonal phase is geometrically described by a set of parameters. These include (1) dihedral, rotation, apical, and equatorial angles of the inorganic framework (see Table S2) and (2) angles defining the orientation of the MA^+ cations. First, we measured these parameters on the surface and internal layers of the slab models. As a reference, we consider reported mean values and their standard deviations for bulk MAPI.[24] The dynamic slab models have the inorganic framework parameters within the reported range for the bulk phase. Thermal motion mainly cancels out the differences in these parameters between the surface layers and bulk (inner) layers. Furthermore, there are no significant differences in the parameters between the two types of slabs. Similar to the dynamic models, the static slab models represent the tetragonal phase, although the apical angle (Pb−I−Pb along the *z* axis) shows deviations.

The orientation of the MA^+ differs significantly at surface and bulk layers. Allow us to consider the angle between the vector representing the C−N bond and the lattice *ab* plane, called polar angle. Figure 7 shows the distributions of polar angles for all the layers of MAPI(001)-MAI and MAPI(001)-PbI_2 slabs. The distributions indicate that the MA^+ tends to have a preferential dipole orientation in the surface layers that disappears in the bulk. For the MAPI(001)-MAI surface, the surface MA^+ has all the CH_3 groups pointing outward (to the vacuum) all the time. On the other hand, for MAPI(001)-PbI_2 surfaces, the subsurface MA^+ presents both orientations, but the higher peak of the distribution corresponds to NH_3^+ groups pointing outward. In this case, it is observed that MA^+ changes its orientations during the trajectory. For inner (bulk) layers under both types of surface, the polar angles are distributed with two almost symmetrical peaks. There is also a surface effect on the inclination of the cation that is independent of the surface termination; the polar angle is 22° in the bulk, while on the surface it is greater than 50° degrees.

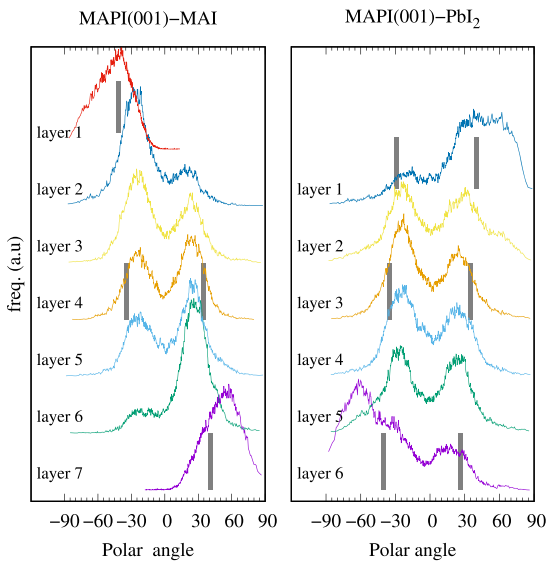

Figure 7. Distributions of C−N polar angles for every layer of MAPI(001)-MAI and MAPI(001)-PbI_2 slabs. Vertical lines indicate the average angles for static slab models.

The static model of MAPI(001)-MAI reproduces the preferred MA^+ orientation in the surface and agrees with previous reports with static[17] and dynamic[16] calculations. These reports associated those changes with weak interactions accounted through vdW functionals and Grimme dispersion correction, respectively. In contrast, we found this MA^+ orientation even without considering the vdW corrections while using the PBEsol functional in convergence studies. We realize that this orientation is maintained by electrostatic interactions and mainly by hydrogen bonds of each surface iodine atom with two nearby cations simultaneously. Hence, each surface iodine atom increases its coordination number, which decreases surface energy and increases surface stability compared to other configurations. Under these interactions, the I−I interatomic distances are significantly reduced compared to the other situations. The dynamic model suggests, as will be discussed later, that it is possible to observe a pattern of rearrangement of iodine atoms at the surface due to these interactions.

The static model of MAPI(001)-PbI_2 does not reflect the trends of the MA^+ orientations observed during the dynamics. In this case, the model in which no MA^+ layer has a net dipole moment (unpolarized slab) corresponds to the conformation of the minimum (internal energy). The formation of polarized slabs, in which all the cations of the first layer have the NH_3^+ group facing outward, is energetically feasible (ΔE = 0.1 eV/MA^+ with respect to the unpolarized slab). In both structures, it is observed that NH_3^+ groups form hydrogen bonds, creating a network of similar interactions with the nearest I atoms. Unlike the MAPI(001)-MAI surface, the MA^+ orientation preference observed in this case as the polarized model could be justified by the electrostatic interaction between NH_3^+ groups and high electronic density in surface (due to the surface states).

Figure 8 shows that both types of MAPI surfaces undergo relaxation along the *c* axis but not in the *ab* plane. There is a reduction in the Pb−I bond distance distribution of the outermost surface layers as compared to the bulk (inner) layers. In the figure, the labels Surf out and Surf in mean the Pb−I distance distributions in the outermost layer (out) and the next closest to it (in), while the Bulk label means the average distribution of two layers in the center of the slab. On average, the difference between Surf out and Surf in is around 0.25 on both types of surfaces. However, the distance Pb−I in MAPI(001)-PbI_2 is reduced by 0.16 with respect to bulk, while this difference is 0.08 for the MAPI(001)-MAI slab. There is no significant difference between the Pb−I average distance in the bulk of both models, as expected. Notice that the corresponding distance of the static models, represented by vertical lines, reproduces the dynamic behavior in the case of the MAPI(001)-PbI_2 slab. The static model of the MAPI(001)-MAI slab hides this surface relaxation phenomenon observed while considering the thermal motion. This means that the static model is one of the possible

https://dx.doi.org/10.1021/acsomega.0c04420
ACS Omega 2020, 5, 29477−29491

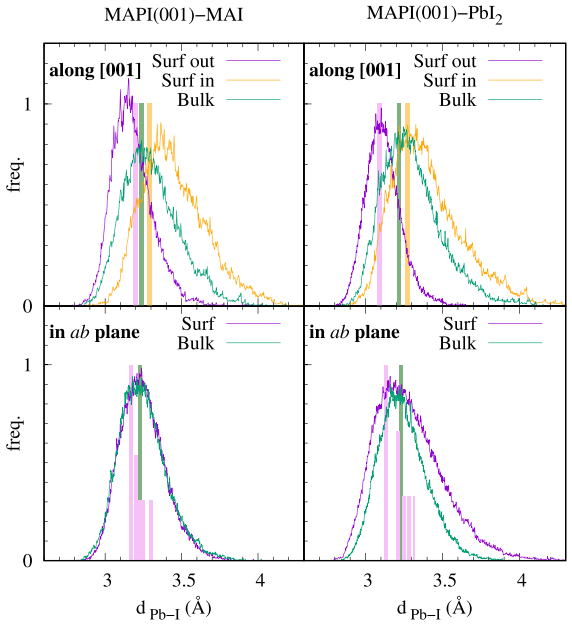

Figure 8. Distributions of the Pb–I bond distances along the [001] direction and parallel to the *ab* plane for MAPI(001)-MAI and MAPI(001)-PbI_2 slabs. Surf out and Surf in refer to the outermost bonds and the next below, respectively. Bulk refers to bonds at slab centers. Vertical lines correspond to the average bond distances of the static slab.

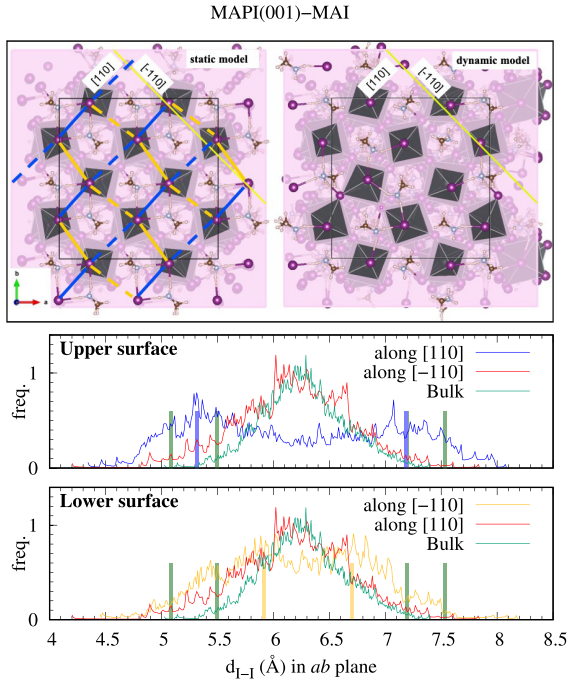

Figure 9. Top left: surface layer of relaxed static slab. Top right: MD snapshot of the surface layer. Bottom: distribution of I–I distances for I atoms in several (001) planes: upper surface, central planes (bulk), and lower surface. Vertical lines are the average I–I distances in static slabs.

configurations that represent the surface properties. However, distorted configurations should be also used to model the surface electronic properties.

As noted above, our MAPI(001)-MAI model also shows regular rearrangements of iodine atoms at the surface compared to those in bulk, which are related to stabilizing interactions with MA^+. According to the I–I distance distributions, the surface layers show iodine arrangements in a certain order depending on the crystallographic orientation on the surface (Figure 9, bottom). In contrast, the iodine atoms in the bulk show a unique (6.2 Å as average) although wide distribution due to thermal motion. During dynamic equilibrium, organic cations experience different orientations within the lattice *ab* plane, and the I–I distance distributions have a maximum at 5.4/7.1 Å in the upper surface and at 5.9/6.7 Å in the lower surface. Perpendicular to these regular distributions, both surfaces show that the iodines are distributed on average at 6.2 Å in wide distributions, as in the bulk. Notice that two different surfaces are obtained for this slab. The surface of the static model (Figure 9, top-left), as ideally ordered reference, allows to understand that, if two iodine atoms share hydrogen bonds with the same cations, then they approach to a distance of 5.4 Å (or move away to 7.1 Å), in average. The rest of the distributions correspond to situations where hydrogen bonds with organic cations are also presented but without a regular order as in a snapshot of the dynamic (Figure 9, top right). Notice that in the static model, the hydrogen bonds are maximized either in the surface or in the bulk. The iodine arrangement patterns found on the surface are consistent with the results obtained from the *in situ* STM experiment of this type of surface but for the low-temperature orthorhombic phase.[7] Despite the limited size of our models, we believe that our evaluation can contribute to the analysis of surface phenomena in similar experiments in the tetragonal phase.

It should be noted that in a convergence study, all thickness models show similar surface structural features as described here for static models. The fact that the geometry of the static models does not show appreciable changes explains the small variations found in the calculated surface energy based on the thickness of the slabs.

Slab Energy Levels and Band Edge Shifts. Hereinafter, we summarize our results on the electronic properties of modeled MAPI(001)-PbI_2 and MAPI(001)-MAI surfaces. First, the electronic structure of static models is described, for which it is feasible to explore different theoretical approaches. Then, given the dynamic models, we can assess the influence of the structural distortions on the slab energy levels and the band energy shifts that may occur.

Figure 10 shows the DOS and the plane-projected DOS for the MAPI(001)-PbI_2 surface comparing the optB88-vdW and HSE+SOC methods. Based on dynamic analysis, we consider adding a static model of this surface that we call polarized. This polarized model is a configuration in which the NH_3^+ groups of the surface layers are oriented outward.

Figure 10 shows the DOS of both models, unpolarized (solid lines) and polarized (dashed lines), to compare. For both methods the HOCO is a surface state (one spin degenerate for each surface). The VB-confined states are below in energy, close to the bulk VBM, as expected from Figure 3. The method optB88-vdW shows more surface states with energies close to VBM, while with HSE+SOC, these surface states are a bit deeper in energy but still close to the VBM. The DOS rises more abruptly near the CBM with optB88-vdW because the neglect of SOC causes the CB to be flat in some directions. The quantum confinement is apparent

https://dx.doi.org/10.1021/acsomega.0c04420
ACS Omega 2020, 5, 29477−29491

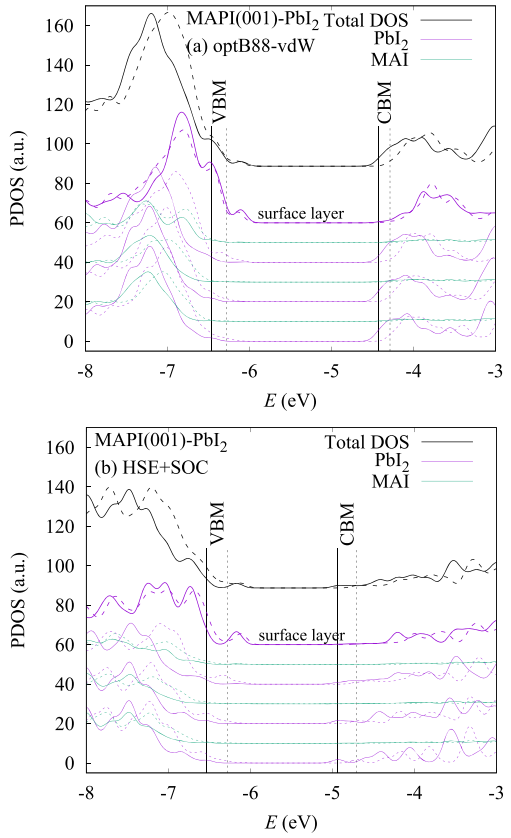

Figure 10. Projected DOS on PbI_2 and MAI layers from the surface to interior, for MAPI(001)-PbI_2 unpolarized (solid lines) and polarized (dashed lines), computed with (a) optB88-vdW and (b) HSE+SOC methods. The energies of bulk VBM and CBM are indicated.

on the CB DOS, the first peak is higher than the bulk CBM, and it is absent in the PDOS on the surface plane. The DOS of the polarized model is quite similar to the corresponding unpolarized one, except that the states of the former are shifted to higher energies.

Table 2 presents a comparison of the energy levels obtained with different approaches: (1) all with the vdW (optB88-vdW) functional, (2) mixed approach combining vdW and hybrid functional with SOC, and (3) all with the hybrid functional with SOC. Let us recall that in the mixed approach, the self-consistent slab calculation has been performed with the vdW functional, from which the term $\overline{V}(z_{in})$ in eq 3 is taken, while the bulk VBM and CBM energies ($E_\alpha^{3D} - \overline{V}^{3D}$) are taken from a hybrid functional calculation HSE+SOC. Also shown are the energies of the slab quantum confined frontier orbitals $E_{VBM,\ CBM}^{slab}$ and the energy of the highest occupied surface state E_{surf} (HOCO), both with the vdW and the hybrid functional. The differences between (2) and (3) are due only to $\overline{V}(z_{in})$, which turns out to be smaller than 0.05 eV; this is a minor difference. Also, for the sake of completeness, we include also results obtained with QE for vdW functional. The differences of (2) and (3) with (1) are large for the VBM and CBM, which is well understood in terms of the famous gap error and the above discussion. Notably, the surface state energy is similar to both functionals. It would be wrong to obtain E_{surf} by applying a correction to the vdW value.

There is other difference between optB88-vdW and HSE+SOC. For a slab made with a single in-plane unit cell, as shown in a previous section, the surface orbitals are the HOCO and HOCO − 1, one for each surface, and each one being doubly degenerate by spin. As the present slab was built from a 2 × 2 surface, the surface orbitals at k = 0 are 8, i.e., from HOCO to HOCO − 7. Six of these orbitals correspond to the high symmetry points $X\left(\frac{1}{2},0,0\right)$, $M\left(\frac{1}{2},\frac{1}{2},0\right)$, and $Y\left(0,\frac{1}{2},0\right)$ of a (1 × 1) surface slab, which fold into the Γ point of the (2 × 2) surface slab. The HOCO − 8 is also a surface state derived from a lower surface band. E_{VBM}^{slab} corresponds to the HOCO − 9 for (2 × 2) in our surface model. In contrast, with HSE+SOC, the (2 × 2) has the quantum-confined VBM as the HOCO − 2, the other surface states having lower energy. This suggests a different dispersion of the surface bands with both functionals. In Table 2, only the highest surface state energy is shown.

Table 2 also shows that the energy difference between the surface states (E_{surf}) of the unpolarized and polarized slab of MAPI(001)-PbI_2 is negligible. There are also negligible band gap differences between these models for the same theoretical level. However, the energy levels of the slab with respect to vacuum change due to variations in the average electrostatic potential within the models. The shift seems to be as large as 0.25 eV, and this could influence band alignments.

Table 2. Band Edges and Slab Energy Levels with Respect to the Vacuum Level for a Slab MAPI(001)-PbI_2 and MAPI(001)-MAI[d]

method	E_{VBM}	E_{CBM}	E_{surf}	E_{VBM}^{slab}	E_{CBM}^{slab}
MAPI(001)-PbI_2 Unpolarized (Polarized)					
optB88-vdW (QE)[c]	−6.49 (−6.22)	−4.60 (−4.33)	−6.13 (−6.06)	−6.48 (−6.22)	−4.51 (−4.29)
optB88-vdW (VASP)[c]	−6.48 (−6.27)	−4.53 (−4.31)	−6.11 (−6.14)	−6.46 (−6.28)	−4.43 (−4.29)
HSE+SOC (VASP)[b]	−6.61 (−6.39)	−5.11 (−4.90)			
HSE+SOC (VASP)[c]	−6.56 (−6.27)	−5.07 (−4.78)	6.18 (−6.12)	−6.54 (−6.28)	−4.94 (−4.71)
MAPI(001)-MAI					
optB88-vdW (QE)[c]	−5.22	−3.33		−5.23	−3.28
optB88-vdW (VASP)[c]	−5.23	−3.27		−5.24	−3.19
HSE+SOC (VASP)[b]	−5.35	−3.86			
HSE+SOC (VASP)[c]	−5.25	−3.76		−5.27	−3.66

[a]To obtain quantum confinement free energies, the quantum-confined correction with SOC for the n = 6 slab model must be added. Δ_{QC} = 0.07 and −0.18 eV for VBM and CBM in the PbI_2 surface. Δ_{QC} = 0.04 and −0.12 eV for VBM and CBM in the MAI surface. [b]Mixed method. [c]Self-consistent. [d]E_{surf} is the energy of top surface states (HOCO). E_{VBM}^{slab} and E_{CBM}^{slab} are the energies of the first quantum confined states[a] of the valence and conduction bands, respectively.

https://dx.doi.org/10.1021/acsomega.0c04420
ACS Omega 2020, 5, 29477−29491

The PDOS for the slab MAPI(001)-MAI is shown in Figure 11. There are no in-gap surface states, both HOCO and

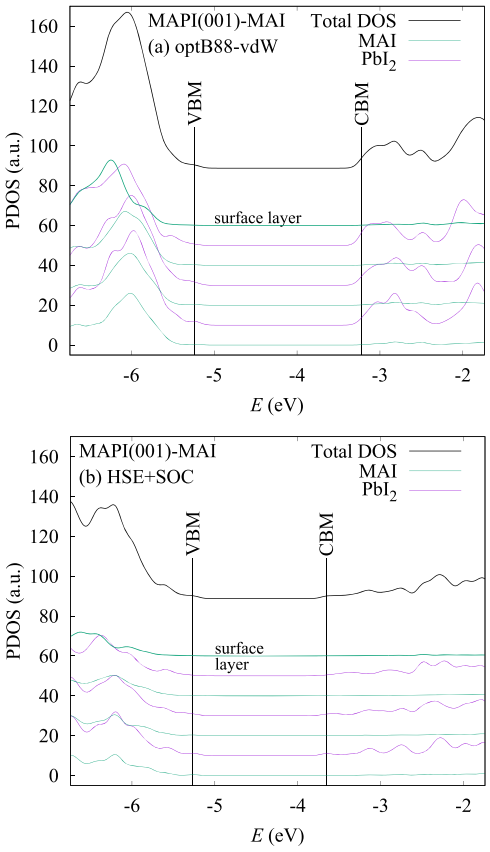

Figure 11. Projected DOS on PbI_2 and MAI layers from the surface to interior, for MAPI(001)-MAI, computed with (a) optB88-vdW and (b) HSE+SOC methods. The energies of bulk VBM and CBM are indicated.

HOCO − 1 are confined states with both functionals. The surface MAI has no contributions at the CB. The PDOS over the CBM shows small differences between the subsurface PbI_2 layer and the inner PbI_2 layers. It is apparent that the first peak around −2.9 eV is slightly increased for the subsurface layer. The difference is better appreciated with the plot of the squared wave functions in Figure 12. The HOCO and HOCO − 1 are practically equal with both functionals. There is some difference for the CB states. With optB88-vdW, all the orbitals from LUCO to LUCO + 4 have important contribution from the subsurface PbI_2 layers. In contrast, with HSE+SOC, the LUCO is clearly a confined state, while LUCO + 1 to LUCO + 3 present mixed confined-subsurface character.

In order to evaluate the shift of slab energy levels due to thermal motion, we use a set of 270 representative configurations of each dynamic slab models, which uncover structural distortions. The self-consistent calculation of each configuration was computed with the VASP code, with the PBE functional including SOC, which implies a reasonable computational cost to give a correct topological description of the edges of the band. Now, we are not interested in the precise values of state energies but in their distributions (band edge shifts) due to the thermal motion.

Figure 13 shows the distributions of the slab energy levels in the dynamic models, and the energies corresponding to the static models are superimposed to compare. All energies were

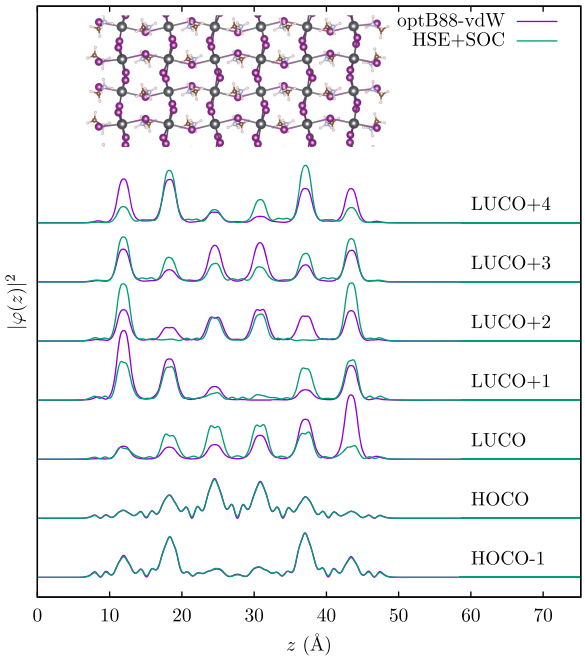

Figure 12. Planar-averaged squared wave functions for MAPI(001)-MAI, computed with optB88-vdW and HSE+SOC methods. The HOCO and HOCO − 1 are plotted with a negative sign.

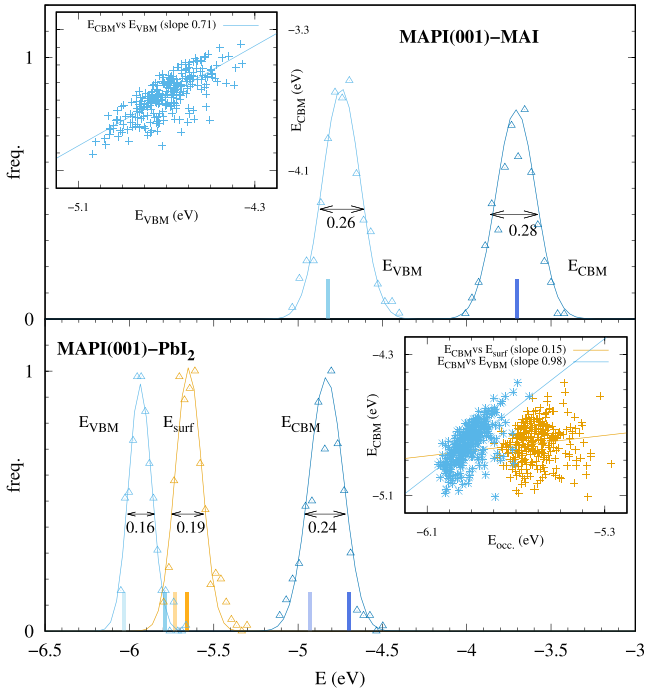

Figure 13. Distributions of the slab energy levels for MAPI(001)-MAI (top) and MAPI(001)-PbI_2 (bottom) dynamic models. Vertical bars show a static model energy level. For MAPI(001)-PbI_2, the light (dark) bars show the levels of the unpolarized (polarized) slab. Insets: CBM vs VBM and surface levels with linear regression.

calculated under the same theoretical approach. In the MAPI(001)-PbI_2 slab, the energy of the surface (E_{surf}) and the conduction band (E_{CBM}) states appear uncorrelated at the Γ point (correlation coefficient = 0.12 with a linear regression fit). In contrast, the energies of the frontier quantum confined states (E_{CBM} vs E_{VBM}) of this slab are rather correlated

https://dx.doi.org/10.1021/acsomega.0c04420
ACS Omega 2020, 5, 29477−29491

(correlation coefficient = 0.63). This explains the broad distribution obtained for the instantaneous band gap $E_{CBM} - E_{surf}$, compared with $E_{CBM} - E_{VBM}$, see Figure 14. In the

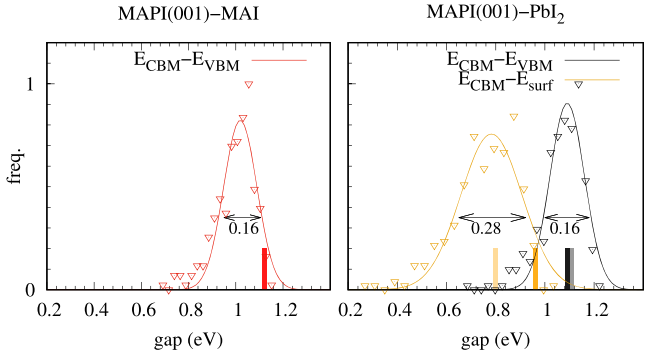

Figure 14. Band gap distributions of the surface dynamic models. Vertical bars show a static model band gap. For MAPI(001)-PbI_2, the light (dark) bars show the levels of the unpolarized (polarized) slab.

MAPI(001)-MAI slab, uncorrelated surface states are not observed either despite the observed surface relaxation. We verify that this also occurs with the occupied state closer to the valence band of the slab (E_{VBM-1}).

The full width at half maximum (FWHM) values of the MAPI(001)-MAI states are larger than those of the MAPI(001)-PbI_2 surface (see Figure 13). Notice that the positions of the band edges in static models (vertical lines) are close to the center of the distributions obtained in the dynamics. Accordingly, the energy levels of each slab model are expected to suffer broadened deviations, i.e., the standard deviation corresponding to each FWHM, due to the thermal motion. Figure 14 also shows a similar average band gap between the confined states on both surfaces, as expected. With thermal motion, the band gap of the MAI-type surface is renormalized by c.a. 0.12 eV. Furthermore, it can be seen that a lower band gap could appear if the MAPI(001)-PbI_2 surface state is considered.

Let us note that molecular dynamics breaks the instantaneous symmetry between the slab surfaces, causing differences in the local vacuum level at each side. We have not applied dipole corrections either during the dynamics with CP2K or for the energy calculation with VASP. Therefore, there is a fluctuating electric field at the vacuum region, which complicates the selection of the vacuum level as a reference for the instantaneous surface and band edge energies. The energies shown in Figure 13 are relative to the instantaneous potential at the center of the vacuum region. This approach is roughly equivalent, for average values, to include dipole corrections and to take the average of the local vacuum levels at both surfaces as a reference. Alternatively, one could obtain the energies with respect to both vacuum levels. This would double the amount of data, modifying the distributions shown in Figure 13, but not the average values. Figure S9 shows that the electric field in the vacuum region fluctuates in both positive and negative directions, thus not breaking the symmetry if a time average is considered. Moreover, the fluctuation of the potential at the vacuum center with respect to the supercell mean potential, which is the reference in CP2K and VASP codes, is 0.06 eV.

A typical practice (in static slab calculations) is to freeze one of the slab surfaces, allowing the other surface to relax. In those cases, where the symmetry is broken (both surfaces are different), exist a net dipole along the slab solvable by means of dipole correction. Figure S10 shows a case example, where the averaged electrostatic potential was calculated with and without dipole corrections. In the first case, there are two vacuum levels, one for each surface. In the second case, there is not an evident vacuum level. It is worth to mention that the average value between both vacuum levels, when the dipole correction is applied, is practically the same as the potential in the middle of the vacuum region, when the dipole correction is not applied.

Finally, we also approximate how the effect of small strain on the slab can affect the energy of its electronic levels. For this we imposed changes of ±4% in the vectors a and b of the supercells, all the details are given in the Supporting Information. We found that the MAI-terminated surface is susceptible to these changes and could experience energy level shifts of up to 0.5 eV in the strain range studied. This is an effect to consider when studying interface alignments.

Implications for Band Alignment. The search for companion materials for different layers in electronic devices is guided by Anderson's rule on band alignment with respect to the vacuum level.[2] A solar cell that uses MAPI as a light absorber requires the electron transport layer (ETL) and MAPI CBMs to be aligned. Meanwhile, the hole transport layer (HTL) and MAPI VBMs also need to be aligned. Values of −5.4 and −3.9 eV for the VBM and CBM energies, respectively, were computed in ref 50, which have been widely used to search HTL and ETL materials.[2,4,5,51] Other values have been measured, showing a distribution of values dependent on the growth technique.[52−54] A clear correlation of the surface composition with the IP and EA has been found.[2,55,56] These measurements match our results for the VBM values obtained for surface layers MAI and PbI_2 displayed in Table 2 and summarized in Figure 15. The figure presents the results of the best theoretical predictions obtained in this work, which are the states obtained with HSE+SOC (VASP) for the slabs including quantum confinement corrections. The surface states of the MAPI(001)-PbI_2 surface in the figure correspond to self-consistent calculations. All these theoretical values in the figure include the standard

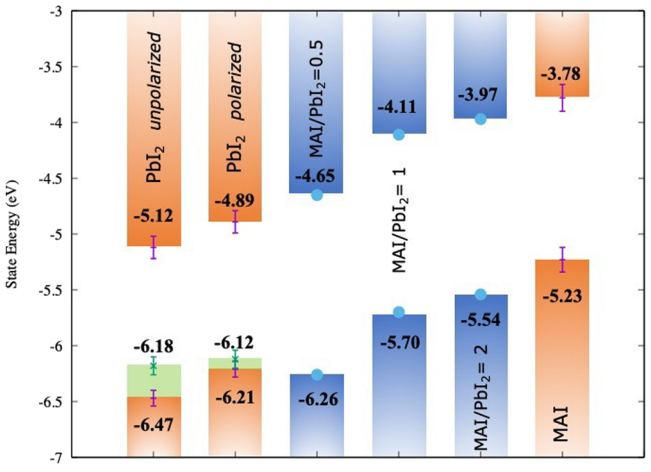

Figure 15. MAPI energy levels for alignment; the best theoretical prediction in this work (orange for bulk and green for surface state edges) considering the thermal broadening and the experimental data depending on the composition (blue).[2,55,56]

https://dx.doi.org/10.1021/acsomega.0c04420
ACS Omega 2020, 5, 29477−29491

deviation (error bars) as a result of thermal motion. Notice that the expected fluctuations for the VBM and CBM levels could significantly influence the alignment between states with small offset.

The energy levels calculated for the MAI-terminated surface match those reported experimentally for the surfaces obtained with MAI/PbI_2 ratios greater than or equal to 1. In addition, these energies correspond to the trend reported for MAPI obtained by solution preparation methods.[3] On the other hand, the energy levels of the PbI_2-terminated surfaces tend to correspond to those reported for MAPI prepared using coevaporation methods.[3] Thus, our models could represent structural models of the MAPI surface depending on the preparation method.

Interestingly, Butler *et al.*[57] made a computational search for HTL and ETL, considering a theoretical value of −5.7 and −4.0 eV for VBM and CBM, respectively,[58] but allowing barrier heights of ±0.5 eV, which turns out to be equivalent to allow the VBM of MAPI to fluctuate in the range −6.2 to −5.2 eV.

On PbI_2-terminated surfaces, the surface states caused by Pb dangling bonds contribute to high reactivity. This reactivity could be used as a driving force for catalytic reactions or to obtain stable interfaces of MAPI with companion materials, e.g., ETL and HTL. If the dangling bonds are not suppressed, then they lead to interface-localized levels. In solar cells, these states can be recombination centers. Completion of Pb-centered octahedra can eliminate or mitigate these recombination centers.[59] For surfaces in humid environment, water molecules are likely to complete the valences of Pb atoms, and the surface is passivated.[16] This condition is detrimental to photocatalytic applications.

CONCLUSIONS

With respect to the DFT methodology, our calculations prove the feasibility of the two-step procedure to refer the bulk VBM and CBM energy levels to the energy scale of the slab. The efficiency of this procedure allows to include the effects of higher precision methods, hybrid functionals, and quasiparticle models to estimate the energy levels of the surfaces. In this line, it is also possible to assess the error in energy levels caused by the usual quantum confinement of the slab models. Here, we propose an analytical function to directly obtain this error as a function of the thickness of the slab.

It is also essential to consider possible surface states (which can only be addressed with self-consistent calculation) that may arise from the incomplete coordination sphere of surface Pb atoms. These states can modify the optical properties and reactivity of the surface and even provide new applications. Furthermore, in the case of this "soft" material, our results show that the surface energy levels are also sensitive to the thermal motion of the structure. In fact, the dynamic models of the MAPI surfaces show that this effect would make it possible to overcome or not energy barriers of up to 0.14 eV, and this would decide the charge transport at the interface.

ASSOCIATED CONTENT

Supporting Information

The Supporting Information is available free of charge at https://pubs.acs.org/doi/10.1021/acsomega.0c04420.

Detailed description of DFT calculation setups; additional information regarding band structure, electrostatic potential profile, plane-averaged wave function profiles for frontier orbitals, *n* energy plots, surface energy convergence, structural information (tetragonal phase), and a strain effect study for PbI_2 and MAI surface models (PDF)

AUTHOR INFORMATION

Corresponding Authors

Lucas Lodeiro − *Departamento de Química, Facultad de Ciencias, Universidad de Chile, Ñuñoa, Santiago 7800003, Chile*; orcid.org/0000-0001-5073-641X; Email: lucas.lodeiro@ug.uchile.cl

Ana L. Montero-Alejo − *Departamento de Física, Facultad de Ciencias Naturales, Matemática y del Medio Ambiente (FCNMM), Universidad Tecnológica Metropolitana, Ñuñoa, Santiago 7800002, Chile*; orcid.org/0000-0003-1675-0546; Phone: +56 (2) 2787 7190; Email: amonteroa@utem.cl

Eduardo Menéndez-Proupin − *Departamento de Física, Facultad de Ciencias, Universidad de Chile, Ñuñoa, Santiago 7800003, Chile*; Phone: +56 (2) 2978 7439; Email: emenendez@uchile.cl; Fax: +56 (2) 2271 2973

Authors

Felipe Barría-Cáceres − *Departamento de Física, Facultad de Ciencias, Universidad de Chile, Ñuñoa, Santiago 7800003, Chile*

Karla Jiménez − *Departamento de Física, Facultad de Ciencias, Universidad de Chile, Ñuñoa, Santiago 7800003, Chile*

Renato Contreras − *Departamento de Química, Facultad de Ciencias, Universidad de Chile, Ñuñoa, Santiago 7800003, Chile*

Complete contact information is available at: https://pubs.acs.org/10.1021/acsomega.0c04420

Notes

The authors declare no competing financial interest.

ACKNOWLEDGMENTS

This work was supported by the ANID/CONICYT/FONDECYT Regular 1150538, 1171807, and Iniciación 11180984 grants. Powered@NLHPC: This research was partially supported by the supercomputing infrastructure of the NLHPC (ECM-02). This work was partially supported by the Ministerio de Economía y Competitividad through the project SEHTOP-QC (ENE2016-77798-C4-4-R). We thank S. Midgley for help with the CP2K code. A.L.M.-A. and F.B.-C. acknowledge the support of Millennium Nucleus MultiMat, Chile.

REFERENCES

(1) NREL *Chart on record cell efficiencies*; https://www.nrel.gov/pv/assets/pdfs/bestresearch-cell-efficiencies.20200925.pdf, (accessed 2020-10-30).

(2) Schulz, P.; Cahen, D.; Kahn, A. Halide Perovskites: Is It All about the Interfaces? *Chem. Rev.* **2019**, *119*, 3349−3417.

(3) Wang, S.; Sakurai, T.; Wen, W.; Qi, Y. Energy Level Alignment at Interfaces in Metal Halide Perovskite Solar Cells. *Adv. Mater. Interfaces* **2018**, *5*, 1800260.

(4) Urieta-Mora, J.; García-Benito, I.; Molina Ontoria, A.; Martín, N. Hole Transporting Materials for Perovskite Solar Cells: A Chemical Approach. *Chem. Soc. Rev.* **2018**, *47*, 8541−8571.

(5) Fakharuddin, A.; Schmidt-Mende, L.; Garcia-Belmonte, G.; Jose, R.; Mora-Sero, I. Interfaces in Perovskite Solar Cells. *Adv. Energy Mater.* **2017**, *7*, 1700623.
(6) Fernandez-Delgado, O.; Castro, E.; Ganivet, C. R.; Fosnacht, K.; Liu, F.; Mates, T.; Liu, Y.; Wu, X.; Echegoyen, L. Variation of Interfacial Interactions in PC61BM-like ElectronTransporting Compounds for Perovskite Solar Cells. *ACS Appl. Mater. Interfaces* **2019**, *11*, 34408−34415.
(7) She, L.; Liu, M.; Zhong, D. Atomic Structures of $CH_3NH_3PbI_3$ (001) Surfaces. *ACS Nano* **2016**, *10*, 1126−1131.
(8) Ohmann, R.; Ono, L. K.; Kim, H.-S.; Lin, H.; Lee, M. V.; Li, Y.; Park, N.-G.; Qi, Y. Real-Space Imaging of the Atomic Structure of Organic Inorganic Perovskite. *J. Am. Chem. Soc.* **2015**, *137*, 16049−16054.
(9) Ono, L. K.; Qi, Y. Surface and Interface Aspects of Organometal Halide Perovskite Materials and Solar Cells. *J. Phys. Chem. Lett.* **2016**, *7*, 4764−4794.
(10) Qiu, L.; He, S.; Ono, L. K.; Qi, Y. Progress of Surface Science Studies on ABX3-Based Metal Halide Perovskite Solar Cells. *Adv. Energy Mater.* **2019**, 1902726.
(11) Dong, Y.; Li, K.; Luo, W.; Zhu, C.; Guan, H.; Wang, H.; Wang, L.; Deng, K.; Zhou, H.; Xie, H.; Bai, Y.; Li, Y.; Chen, Q. The Role of Surface Termination in Halide Perovskites for Efficient Photocatalytic Synthesis. *Angew. Chemie Int. Ed.* **2020**, *59*, 12931−12937.
(12) Wang, Y.; Sumpter, B. G.; Huang, J.; Zhang, H.; Liu, P.; Yang, H.; Zhao, H. Density Functional Studies of Stoichiometric Surfaces of Orthorhombic Hybrid Perovskite $CH_3NH_3PbI_3$. *J. Phys. Chem. C* **2015**, *119*, 1136−1145.
(13) Torres, A.; Rego, L. G. C. Surface Effects and Adsorption of Methoxy Anchors on Hybrid Lead Iodide Perovskites: Insights for Spiro-MeOTAD Attachment. *J. Phys. Chem. C* **2014**, *118*, 26947−26954.
(14) Haruyama, J.; Sodeyama, K.; Han, L.; Tateyama, Y. Termination Dependence of Tetragonal $CH_3NH_3PbI_3$ Surfaces for Perovskite Solar Cells. *J. Phys. Chem. Lett.* **2014**, *5*, 2903−2909.
(15) Geng, W.; Tong, C.-J.; Tang, Z.-K.; Yam, C.; Zhang, Y.-N.; Lau, W.-M.; Liu, L.-M. Effect of Surface Composition on Electronic Properties of Methylammonium Lead Iodide Perovskite. *J. Materiomics* **2015**, *1*, 213−220.
(16) Mosconi, E.; Azpiroz, J. M.; De Angelis, F. *Ab Initio* Molecular Dynamics Simulations of Methylammonium Lead Iodide Perovskite Degradation by Water. *Chem. Mater.* **2015**, *27*, 4885−4892.
(17) Quarti, C.; De Angelis, F.; Beljonne, D. Influence of Surface Termination on the Energy Level Alignment at the $CH_3NH3_pbI_3$ Perovskite/C_{60} Interface. *Chem. Mater.* **2017**, *29*, 958−968.
(18) Montero-Alejo, A. L.; Menéndez-Proupin, E.; Palacios, P.; Wahnón, P.; Conesa, J. C. Ferroelectric Domains May Lead to Two-Dimensional Confinement of Holes, but not of Electrons, in $CH_3NH_3PbI_3$ Perovskite. *J. Phys. Chem. C* **2017**, *121*, 26698−26705.
(19) Giannozzi, P.; et al. Quantum ESPRESSO: A Modular and Open-Source Software Project for Quantum Simulations of Materials. *J. Phys.: Condens. Matter* **2009**, *21*, 395502.
(20) Perdew, J. P.; Ruzsinszky, A.; Csonka, G. I.; Vydrov, O. A.; Scuseria, G. E.; Constantin, L. A.; Zhou, X.; Burke, K. Restoring the Density-Gradient Expansion for Exchange in Solids and Surfaces. *Phys. Rev. Lett.* **2008**, *100*, 136406.
(21) Klimeš, J.; Bowler, D. R.; Michaelides, A. Van der Waals Density Functionals Applied to Solids. *Phys. Rev. B* **2011**, *83*, 195131.
(22) Klimeš, J.; Bowler, D. R.; Michaelides, A. Chemical Accuracy for the Van der Waals Density Functional. *J. Phys.: Condens. Matter* **2010**, *22*, No. 022201.
(23) Menéndez-Proupin, E.; Palacios, P.; Wahnón, P.; Conesa, J. C. Self-Consistent Relativistic Band Structure of the $CH_3NH_3PbI_3$ Perovskite. *Phys. Rev. B* **2014**, *90*, 045207.
(24) Montero-Alejo, A. L.; Menéndez-Proupin, E.; Hidalgo-Rojas, D.; Palacios, P.; Wahnón, P.; Conesa, J. C. Modeling of Thermal Effect on the Electronic Properties of Photovoltaic Perovskite $CH_3NH_3PbI_3$: The Case of Tetragonal Phase. *J. Phys. Chem. C* **2016**, *120*, 7976−7986.
(25) Kawamura, Y.; Mashiyama, H.; Hasebe, K. Structural study on Cubic-Tetragonal Transition of $CH_3NH_3PbI_3$. *J. Phys. Soc. Jpn.* **2002**, *71*, 1694−1697.
(26) Neugebauer, J.; Scheffler, M. Adsorbate-substrate and adsorbate-adsorbate interactions of Na and K adlayers on Al(111). *Phys. Rev. B* **1992**, *46*, 16067−16080.
(27) Bengtsson, L. Dipole correction for surface supercell calculations. *Phys. Rev. B* **1999**, *59*, 12301−12304.
(28) Heyd, J.; Scuseria, G. E.; Ernzerhof, M. Hybrid Functionals Based on a Screened Coulomb Potential. *J. Chem. Phys.* **2003**, *118*, 8207−8215.
(29) Heyd, J.; Scuseria, G. E.; Ernzerhof, M. Erratum: "Hybrid Functionals Based on a Screened Coulomb Potential". *J. Chem. Phys.* **2006**, *124*, 219906.
(30) Kresse, G.; Furthmüller, J. Efficiency of Ab-Initio Total Energy Calculations for Metals and Semiconductors Using a Plane-Wave Basis Set. *Comput. Mater. Sci.* **1996**, *6*, 15.
(31) Kresse, G.; Furthmüller, J. Efficient Iterative Schemes for Ab Initio Total-Energy Calculations Using a Plane-Wave Basis Set. *Phys. Rev. B* **1996**, *54*, 11169−11186.
(32) Hutter, J.; Iannuzzi, M.; Schiffmann, F.; VandeVondele, J. CP2K: Atomistic Simulations of Condensed Matter Systems. *Wiley Interdiscip. Rev.: Comput. Mol. Sci.* **2014**, *4*, 15−25.
(33) The CP2K developers group. 2018 CP2K is freely available from https://www.cp2k.org
(34) VandeVondele, J.; Krack, M.; Mohamed, F.; Parrinello, M.; Chassaing, T.; Hutter, J. Quickstep: Fast and Accurate Density Functional Calculations Using a Mixed Gaussian and Plane Waves Approach. *Comput. Phys. Commun.* **2005**, *167*, 103−128.
(35) Grimme, S.; Ehrlich, S.; Goerigk, L. Effect of the Damping Function in Dispersion Corrected Density Functional Theory. *J. Comput. Chem.* **2011**, *32*, 1456−1465.
(36) Grimme, S.; Antony, J.; Ehrlich, S.; Krieg, H. A Consistent and Accurate *Ab Initio* Parametrization of Density Functional Dispersion Correction (DFT-D) for the 94 Elements H-Pu. *J. Chem. Phys.* **2010**, *132*, 154104.
(37) Baldereschi, A.; Baroni, S.; Resta, R. Band Offsets in Lattice-Matched Heterojunctions: a Model and First-Principles Calculations for GaAs/AlAs. *Phys. Rev. Lett.* **1988**, *61*, 734−737.
(38) Dandrea, R. G.; Duke, C. B.; Zunger, A. Interfacial Atomic Structure and Band Offsets at Semiconductor Heterojunctions. *J. Vac. Sci. Technol., B* **1992**, *10*, 1744−1753.
(39) Dandrea, R. G.; Duke, C. B. Calculation of the Schottky Barrier Height at the Al/GaAs(001) Heterojunction: Effect of Interfacial Atomic Relaxations. *J. Vac. Sci. Technol., A* **1993**, *11*, 848−853.
(40) Das, T.; Rocquefelte, X.; Jobic, S. Ab Initio Positioning of the Valence and Conduction Bands of Bulk Photocatalysts: Proposition of Absolute Reference Energy. *J. Phys. Chem. C* **2020**, *124*, 19426−19434.
(41) Tran, R.; Li, X.-G.; Montoya, J. H.; Winston, D.; Persson, K. A.; Ong, S. P. Anisotropic work function of elemental crystals. *Surf. Sci.* **2019**, *687*, 48−55.
(42) Adamo, C.; Barone, V. Toward Reliable Density Functional Methods without Adjustable Parameters: The PBE0 Model. *J. Chem. Phys.* **1999**, *110*, 6158−6170.
(43) Perdew, J. P.; Ernzerhof, M.; Burke, K. Rationale for Mixing Exact Exchange with Density Functional Approximations. *J. Chem. Phys.* **1996**, *105*, 9982−9985.
(44) Yu, P. Y.; Cardona, M. *Fundamentals of Semiconductors*; 2nd ed.; Springer: Berlin, 1996; DOI: 10.1007/978-3-662-03313-5.
(45) Yamamuro, O.; Matsuo, T.; Suga, H.; David, W. I. F.; Ibberson, R. M.; Leadbetter, A. J. Neutron Diffraction and Calorimetric Studies of Methylammonium Iodide. *Acta Crystallogr., Sect. B: Struct. Sci.* **1992**, *48*, 329−336.
(46) Persson, K. *Materials Data on H6CIN (SG:11) by Materials Project*. 2016.
(47) Persson, K. *Materials Data on H6CIN (SG:57) by Materials Project*. 2016.

https://dx.doi.org/10.1021/acsomega.0c04420
ACS Omega 2020, 5, 29477−29491

(48) Palosz, B.; Steurer, W.; Schulz, H. The Structure of PbI_2 Polytypes 2H and 4H: A Study of the 2H - 4H Transition. *J. Phys.: Condens. Matter* **1990**, *2*, 5285−5295.
(49) Blancon, J.-C.; et al. Scaling law for excitons in 2D perovskite quantum wells. *Nat. Commun.* **2018**, *9*, 2254.
(50) Even, J.; Pedesseau, L.; Jancu, J.-M.; Katan, C. Importance of SpinOrbit Coupling in Hybrid Organic/Inorganic Perovskites for Photovoltaic Applications. *J. Phys. Chem. Lett.* **2013**, *4*, 2999−3005.
(51) Wang, Y.; Yue, Y.; Yang, X.; Han, L. Toward Long-Term Stable and Highly Efficient Perovskite Solar Cells via Effective Charge Transporting Materials. *Adv. Energy Mater.* **2018**, *8*, 1800249.
(52) Endres, J.; Egger, D. A.; Kulbak, M.; Kerner, R. A.; Zhao, L.; Silver, S. H.; Hodes, G.; Rand, B. P.; Cahen, D.; Kronik, L.; Kahn, A. Valence and Conduction Band Densities of States of Metal Halide Perovskites: A Combined Experimental-Theoretical Study. *J. Phys. Chem. Lett.* **2016**, *7*, 2722−2729.
(53) Olthof, S.; Meerholz, K. Substrate-Dependent Electronic Structure and Film Formation of $MAPbI_3$ Perovskites. *Sci. Rep.* **2016**, *7*, 40267.
(54) Wang, H.; Guerrero, A.; Bou, A.; Al Mayouf, A.; Bisquert, J. Kinetic and Material Properties of Interfaces Governing Slow Response and Long Timescale Phenomena in Perovskite Solar Cells. *Energy Environ. Sci.* **2019**, *12*, 2054−2079.
(55) Kim, T. G.; Seo, S. W.; Kwon, H.; Hahn, J.; Kim, J. W. Influence of Halide Precursor Type and Its Composition on the Electronic Properties of Vacuum Deposited Perovskite Films. *Phys. Chem. Chem. Phys.* **2015**, *17*, 24342−24348.
(56) Emara, J.; Schnier, T.; Pourdavoud, N.; Riedl, T.; Meerholz, K.; Olthof, S. Impact of Film Stoichiometry on the Ionization Energy and Electronic Structure of $CH_3NH_3PbI_3$ Perovskites. *Adv. Mater.* **2016**, *28*, 553−559.
(57) Butler, K. T.; Kumagai, Y.; Oba, F.; Walsh, A. Screening Procedure for Structurally and Electronically Matched Contact Layers for High-Performance Solar Cells: Hybrid Perovskites. *J. Mater. Chem. C* **2016**, *4*, 1149−1158.
(58) Butler, K. T.; Frost, J. M.; Walsh, A. Band Alignment of the Hybrid Halide Perovskites $CH_3NH_3PbCl_3$, $CH_3NH_3PbBr_3$ and $CH_3NH_3PbI_3$. *Mater. Horiz.* **2015**, *2*, 228−231.
(59) Castellanos-Águila, J. E.; Lodeiro, L.; Menéndez-Proupin, E.; Montero-Alejo, A. L.; Palacios, P.; Conesa, J. C.; Wahnón, P. Atomic-Scale Model and Electronic Structure of $Cu_2O/CH_3NH_3PbI_3$ Interfaces in Perovskite Solar Cells. *ACS Appl. Mater. Interfaces* **2020**, *12*, 44648−44657.

https://dx.doi.org/10.1021/acsomega.0c04420
ACS Omega 2020, 5, 29477−29491